Transient experiments on oxidation and degradation of Cr-coated Zircaloy in steam up to 1600 ℃

Junkai Liu [a,b,*], Chongchong Tang [a], Martin Steinbrück [a], Jianqiao Yang [c], Ulrike Stegmaier [a], Mirco Große [a], Di Yun [b,c], Hans Jürgen Seifert [a]

[a] Institute for Applied Materials (IAM), Karlsruhe Institute of Technology (KIT), D-76021 Karlsruhe, Germany
[b] School of Nuclear Science and Technology, Xi'an Jiaotong University, Xi'an 710049, China
[c] Key Laboratory of Thermo-Fluid Science and Engineering of MOE, School of Energy and Power Engineering, Xi'an Jiaotong University, Xi'an 710049, China

Keywords:
ATF cladding
Cr coating
High-temperature steam oxidation
Hydrogen release
Microstructural evolution
Failure behavior

A B S T R A C T

The transient oxidation behavior of magnetron-sputtered chromium-coated Zircaloy-4 was studied in steam up to 1600 °C, and the microstructural evolution of the coating-substrate system after oxidation was investigated. Coating failure and corresponding rapid oxidation of coating and substrate occurred at 1300–1400 °C. It was mainly caused by the thickness decrease of the outer dense Cr_2O_3 scale, the Zr—Cr eutectic reaction, the Zr—Cr interdiffusion, and the precipitation of ZrO_2 along unoxidized Cr grain boundaries. The phase transformation of tetragonal ZrO_{2-x} to cubic ZrO_{2-y} increased the oxidation rate of the Zircaloy-4 substrate at ~1500 °C through the higher oxygen diffusion coefficient in the cubic phase.

1. Introduction

Accident-tolerant fuel (ATF) materials came into the focus of international research after the Fukushima nuclear power plant accidents in 2011 to deal with loss-of-coolant accidents (LOCA) and more severe accidents in the nuclear industry [1–3]. Zirconium alloys with protective surface coating are considered as one of the most promising ATF cladding candidate materials. In recent years, different types of coatings including metallic coatings [4–7], oxide coatings [8,9], nitride coatings [10,11], and MAX phase coatings [12,13] have been deposited on Zircaloy substrate. The performance of these coatings, especially the high-temperature steam oxidation behavior, were comprehensively investigated. Among these concepts of coatings, Cr is considered as the best choice for the surface coating of Zircaloy owing to its optimal oxidation and corrosion resistance and other excellent properties such as thermo-mechanical properties, low thermal expansion coefficient difference with Zr, and favorable irradiation resistance [2,7,14–17]. The oxidation behavior and the oxidation mechanism of the Zircaloy with surface Cr coating deposited by different techniques have been extensively studied under steam atmospheres at temperature up to 1200 °C [6,7,14–16,18]. All these results indicated that surface Cr coatings can significantly improve the oxidation resistance of the Zircaloy substrate by forming a dense and protective Cr_2O_3 layer which inhibits the inward diffusion of oxygen.

Nevertheless, up to date, many uncertainties still exist about the failure mechanism of the Cr coating on Zircaloy substrate during high-temperature steam oxidation. Brachet et al. [7] proposed a mechanism of the microstructural transition between protective and non-protective coating based on the outward diffusion of Zr from the substrate to the Cr coating and its oxidation along the Cr grain boundaries. These ZrO_2 paths increased the inward diffusion of oxygen and caused the oxidation kinetics transition. However, in this work the microstructural evolution and the failure mechanism of the outer dense Cr_2O_3 scale was not discussed in detail. Han et al. [6,18] discovered the thickness decrease of the Cr_2O_3 scale during steam oxidation and they suggested that the outward diffusing Zr reacted with Cr_2O_3 and led to the reduction of Cr_2O_3 to Cr and the formation of ZrO_2. However, the outward diffused Zr in Cr coating was more likely oxidized into ZrO_2 by the oxygen which is dissolved in the coating or diffused from the outer surface of the coating through the Cr_2O_3 grain boundaries [7]. This statement was also verified in our previous work about the steam oxidation of the CrN coating [10], that ZrO_2 precipitates formed close to the coating/substrate interface which was far from the outer Cr_2O_3 layer. The inward diffusion and dissolution of Cr in the Zr substrate can affect the structure integrity of the coating [19]. Besides, the volatilization of the dense Cr_2O_3 scale is a factor that may affect the structural integrity of the coating during steam

* Corresponding author at: Institute for Applied Materials (IAM), Karlsruhe Institute of Technology (KIT), D-76021 Karlsruhe, Germany.
E-mail address: k611478@stu.xjtu.edu.cn (J. Liu).

oxidation at very high temperatures [14], but it was also reported that the volatilization of Cr_2O_3 scale can be neglected up to at least 1300 °C [7]. Therefore, the failure behavior of the coating needs to be investigated further and all the effects of the above factors on the coating failure mechanism need to be comprehensively considered.

Moreover, most of the current steam oxidation tests focus on LOCA conditions up to 1200 °C, and data are missing for beyond design-basis accident environment in which the reactor core temperature is much higher than 1200 °C [20]. The Cr—Zr eutectic reaction at ~1332 °C [7] significantly affects the coating microstructure [21,22] and defines the upper limit for the long-term protective effect of the Cr coatings. Also at such a high temperature, the diffusion coefficients of Cr, O, and Zr are remarkably enlarged, and other transport mechanisms occur in melts, which are produced by the Cr—Zr eutectic reaction. Hence, in very high temperature steam, there are still many questions remaining that need further investigations, for instance how the microstructure of the Cr coating evolves, how the Zircaloy substrate develops, and how the coating failure occurs.

In the current study, a Cr coating with thickness ~17 μm was deposited on the Zircaloy-4 (Zry-4) substrate by magnetron sputtering. Transient steam oxidation tests were conducted at temperature from 600 to a very high temperature up to 1600 °C with a low heating rate of 10 K/min. The hydrogen release during the oxidation was in situ analyzed, and the microstructure characterization of the Cr-coated samples after oxidation was conducted. The oxidation behavior and microstructural evolution of the coating, inward diffusion behavior of Cr in substrate, oxidation of the Zry-4 substrate, and the coating failure mechanism were studied in this paper.

2. Materials and methods

All Cr coatings on the Zry-4 samples were deposited by magnetron sputtering (Oerlikon Company, Bingen, Germany) with a designed thickness of 17 μm. Zry-4 samples (Zr-1.5Sn-0.2Fe-0.1Cr) used in this experiments were in plate shape (15 mm × 10 mm × 0.65 mm) which were cut from commercial Zry-4 plates. On each sample a hole with diameter 2 mm was drilled close to the edge for suspension of the samples in the furnace. All surfaces of the Zry-4 plates including the surfaces of cutting planes and drilling hole were coated by Cr. The oxidation behavior of the bare and the Cr-coated Zry-4 samples was tested in a horizontal tube furnace, called "BOX" rig, which contains a gas and steam supply system (Bronkhorst®), the furnace with alumina reaction tube, and a quadrupole mass spectrometer (MS, IPI GAM3000). This system was introduced in our previous work in detail [23]. Fig. 1 shows the schematic of the furnace part used in the current tests. As shown in Fig. 1, a sample lock was applied allowing for the exchange of samples at high temperature and their fast cool-down. The samples were suspended from a ceramic stick, which was connected with the sample lock.

The transient oxidation tests were conducted in a mixture of steam and argon gas flow starting from 600 °C with a heating rate of 10 K/min to the final temperature ranging from 1200 °C to 1600 °C. The schematic temperature curves for each test during the steam oxidation are shown in Fig. 2. When the temperature in the furnace reached 600 °C, samples were moved into the furnace tube and steam with mass flow 20 g/h was injected into the furnace. The steam with a mass flow of 20 g/h is sufficient to prevent steam starvation during the experiments. When the temperature had reached the pre-defined maximum value, the steam injection was stopped and the samples were pulled out into the sample lock and quenched in flowing argon. The cool-down curves in Fig. 2 are not the true value during the tests but just show that temperature changes are much faster (> 100 K/min at the initial stage of cooling down) than that in the transient oxidation stage. The argon flow during the oxidation and cooling stage was always 20 L/h. The gas produced by the oxidation reaction in the furnace was in situ analyzed by the MS that is connected with the outlet of the furnace. Both the weights of samples before and after oxidation were measured by an analytical balance with an accuracy of 0.1 mg.

X-ray diffraction (XRD, Seifert PAD II diffractometer) and scanning electron microscopy (SEM, PhilipsXL30S) were utilized to study the surface phases and the surface microstructures of the Cr-coated Zry-4 samples before and after oxidation. The XRD signals were collected through CuKα radiation (λ 1.54 Å) in Bragg–Brentano geometry with 40 kV voltage and 30 mA current. Optical microscopy (OM, Reichert-Jung MeF3), SEM, and energy dispersive X-ray spectroscopy (EDS) were used to characterize the cross-sectional microstructures of the Cr-coated Zry-4 samples before and after steam oxidation. All the samples for cross-sectional characterization were first embedded in epoxy resin and then ground and polished.

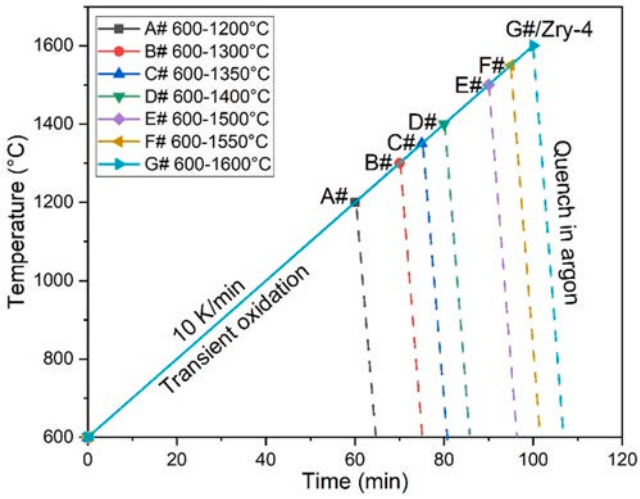

Fig. 2. Schematic temperature profiles during transient steam oxidation tests.

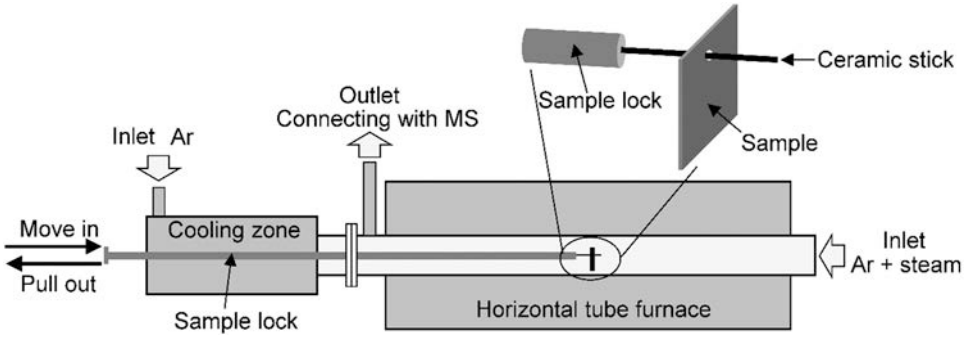

Fig. 1. Schematic diagram of the horizontal tube furnace with the sample lock system and the hanging way of the sample in furnace.

3. Results

3.1. Hydrogen release during transient steam oxidation

Fig. 3(a) shows the transient hydrogen flow rate (per unit area) curves versus oxidation temperature (T, and later in the text T_{max} for the final temperatures of the tests) of seven Cr-coated Zry-4 samples and the bare Zry-4 sample. There is no obvious hydrogen flow rate variation of the Cr-coated samples at T < 1000 °C, so the abscissa begins at 1000 °C to improve the readability of the diagram. As can be seen in Fig. 3(a), all these seven hydrogen flow rate curves of the Cr-coated samples are reproducible and in similar trends. Fig. 3(b) shows the integrated hydrogen release of the coated and the bare Zry-4 samples during the oxidation process and the weight gain of six Cr-coated Zry-4 samples (the G# and bare Zry-4 samples were broken after oxidation, so the post-test weight could not be determined). The variation trends of the weight gain and the integrated hydrogen release are in good agreement in Fig. 3 (b). The integrated H_2 release and weight gain values in Fig. 3(b) are listed in Table 1.

In the early stage of the steam oxidation (T ≤ 1350 °C), the transient hydrogen flow rates (Fig. 3(a)) and the integrated hydrogen release (Fig. 3(b)) of the Cr-coated samples are all much lower than those of the bare Zry-4 sample, which indicates the excellent oxidation resistance of the surface Cr coating. From approx. 1350 °C, the hydrogen release rate, i.e. the oxidation rate of the coated samples, is higher than that of the non-coated reference sample. However, the surface Cr coating reduces

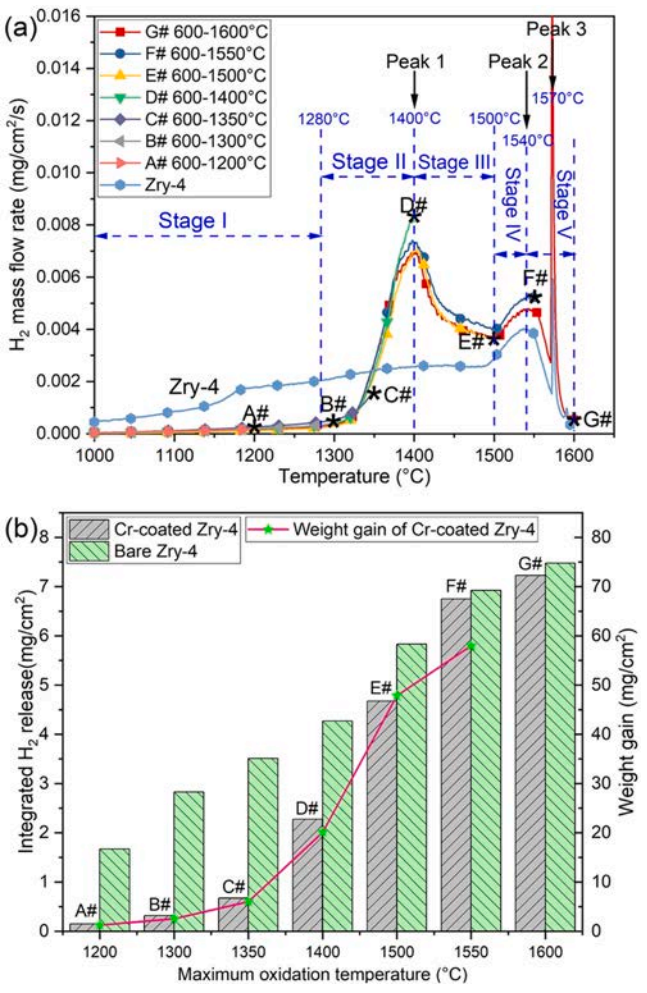

Fig. 3. Hydrogen release behavior of coated and uncoated samples: (a) the transient hydrogen mass flow rate and (b) the integrated hydrogen release and weight gain.

Table 1
The integrated H_2 release and weight gain values in Fig. 3(b).

T_{max} (°C)	1200	1300	1350	1400	1500	1550	1600
IHR of Cr-coated Zry-4 (mg/cm^2)	0.2	0.3	0.7	2.3	4.7	6.8	7.2
IHR of bare Zry-4 (mg/cm^2)	1.7	2.8	3.5	4.3	5.8	6.9	7.5
WG of Cr-coated Zry-4 (mg/cm^2)	1.3	2.6	6.0	20.1	47.9	58.0	/

IHR is integrated H_2 release.
WG is weight gain.

the total hydrogen release of the Zry-4 sample during steam oxidation up to 1500 °C (Fig. 3(b)). In the later stage (1550 ≤ T ≤ 1600 °C), the transient hydrogen flow rate of the bare Zry-4 is only slightly lower than that of the coated samples while the integral values of hydrogen release of the bare Zry-4 is slightly higher than that of the coated Zry-4.

Three hydrogen release peaks of the Cr-coated samples are seen during the whole oxidation process at temperature from 600 °C to 1600 °C in Fig. 3(a): the peak 1 at ~1400 °C; the peak 2 at ~1540 °C; and the sharp peak 3 at ~1570 °C. In comparison, only the last two peaks are detected in the hydrogen flow rate curve of the bare Zry-4 sample. It is worth mentioning that the G# (Fig. 5(h)) and the bare Zry-4 samples broke to pieces during oxidation, which is thought to be the reason for the appearance of the third sharp peak. According to the three peaks and the variation trends of the hydrogen flow rate curves, the oxidation process of the coated Zry-4 can be divided into five stages as shown in Fig. 3(a):

1) **Stage I**: 600–1280 °C. In this stage the hydrogen release increases linearly with temperature, and the oxidation reaction rate is relatively low.
2) **Stage II**: 1280–1400 °C. A transition occurs at this stage and the hydrogen flow rate increases rapidly with the rising of temperature. The hydrogen flow rate reaches its peak at 1400 °C.
3) **Stage III**: 1400–1500 °C. The hydrogen flow rate decreases with the increase of temperature and reaches the curve valley at 1500 °C.
4) **Stage IV**: 1500–1540 °C. The second rise stage of the hydrogen flow rate.
5) **Stage V**: 1540–1600 °C. The second fall stage of the hydrogen flow rate curve and the third peak.

3.2. XRD patterns of the Cr-coated Zry-4 samples before and after oxidation

Fig. 4 shows the XRD patterns of the as-deposited Cr coating and the Cr-coated Zry-4 samples after steam oxidation. The diffraction information comes from the surface of the samples (diffraction depth is only a few micrometers) because of the low penetration depth of the X-ray. Only the peaks of cubic Cr (c-Cr) phase are detected in the as-deposited Cr coating and these peaks completely disappear in the E#, F#, and G # samples with T_{max} ≥ 1500 °C. All the oxidation products of the Cr coating at different temperatures are hexagonal Cr_2O_3 (h-Cr_2O_3) phase and no other oxide of Cr is observed. Low intensity diffraction peaks of monoclinic ZrO_2 (m-ZrO_2) phase and tetragonal ZrO_2 (t-ZrO_2) phase emerge in the D#–G# samples when T_{max} rise to 1400 °C.

3.3. The surface microstructures

Photos of the Cr-coated Zry-4 samples before and after oxidation are displayed in Fig. 5. As the oxidation temperature rises, the surface roughness of the samples increases. At T_{max} < 1400 °C, lusters are seen on the surface of the A#, B#, and C# samples. These lusters disappear on the surface of the D#–G# samples. At temperatures from 1350 °C, ridges (indicated by yellow arrows) form on the surface of the samples, being more obvious at T_{max} > 1350 °C. The surface structure is similar for the

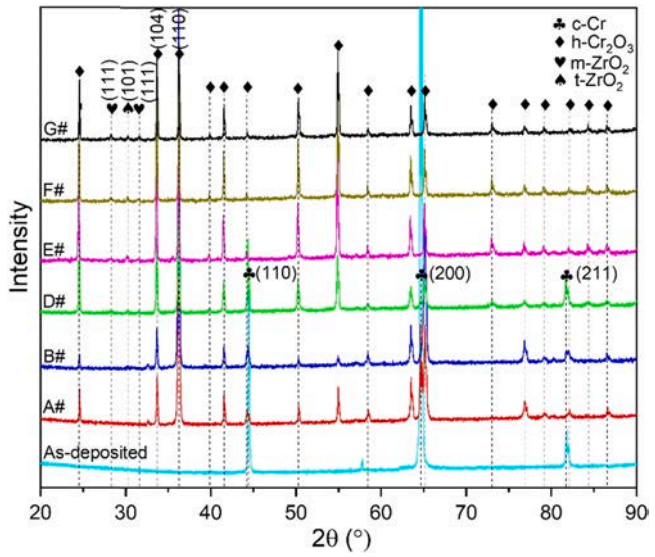

Fig. 4. X-ray diffraction patterns of the as-deposited Cr coating and the Cr-coated Zry-4 samples after steam oxidation.

D#, E#, and F# samples. The G# sample broke to pieces after steam oxidation.

Fig. 6 shows the surface SEM micrographs of the as-deposited Cr coating and the Cr-coated Zry-4 samples after steam oxidation. In Fig. 6 (a), the average grain size of the as-deposited Cr coating is about 2 μm, but the grain size is non-uniform. Also, the surface of the as-deposited Cr coating is uneven with large-sized grains protruding. The surface of the A# (Fig. 6(b)) and B# (Fig. 6(c)) samples is flat and smooth, and no cracks are observed on the surface. When temperature rises to 1400 °C (D# sample in Fig. 6(d)), the smooth surface transforms to a rough one. This is the reason why the surface luster disappears at 1400 °C in Fig. 5. Cracks and nano-sized pores form on the surface of the E# (Fig. 6(e)) and the F# (Fig. 6(f)) samples after being oxidized up to 1500 °C and 1550 °C, respectively. The surface microstructure of the G# sample is similar with the F# sample and no big differences are found.

3.4. The cross-sectional microstructures

3.4.1. The cross-sectional microstructures of the Zry-4 substrate

Fig. 7 shows the cross-sectional OM images of the Cr-coated Zry-4 samples before and after transient steam oxidation. The further SEM and EDS characterizations of the cross-sectional microstructures of several representative samples are shown in Fig. 8. The microstructural evolution of the Zry-4 substrate can be summarized as follows:

1) **The surface**. The surface of the samples is smooth and flat for $T_{max} < 1350$ °C (Fig. 7(a) and (b)), but the surface transforms into a fluctuant and rough one at $T_{max} \geq 1350$ °C (Fig. 7(c)–(f),and (i)). This phenomenon is consistent with the appearance of the ridges on the surface of the C#–G# samples in Fig. 5, which is most probably due to the liquid phase formation during the Zr—Cr eutectic reaction.
2) **The oxide layer**. As can be seen in Fig. 7(a)–(c), the substrate is well protected from oxidation by the outer coating whose structural integrity is not destroyed at temperatures up to 1350 °C. However,

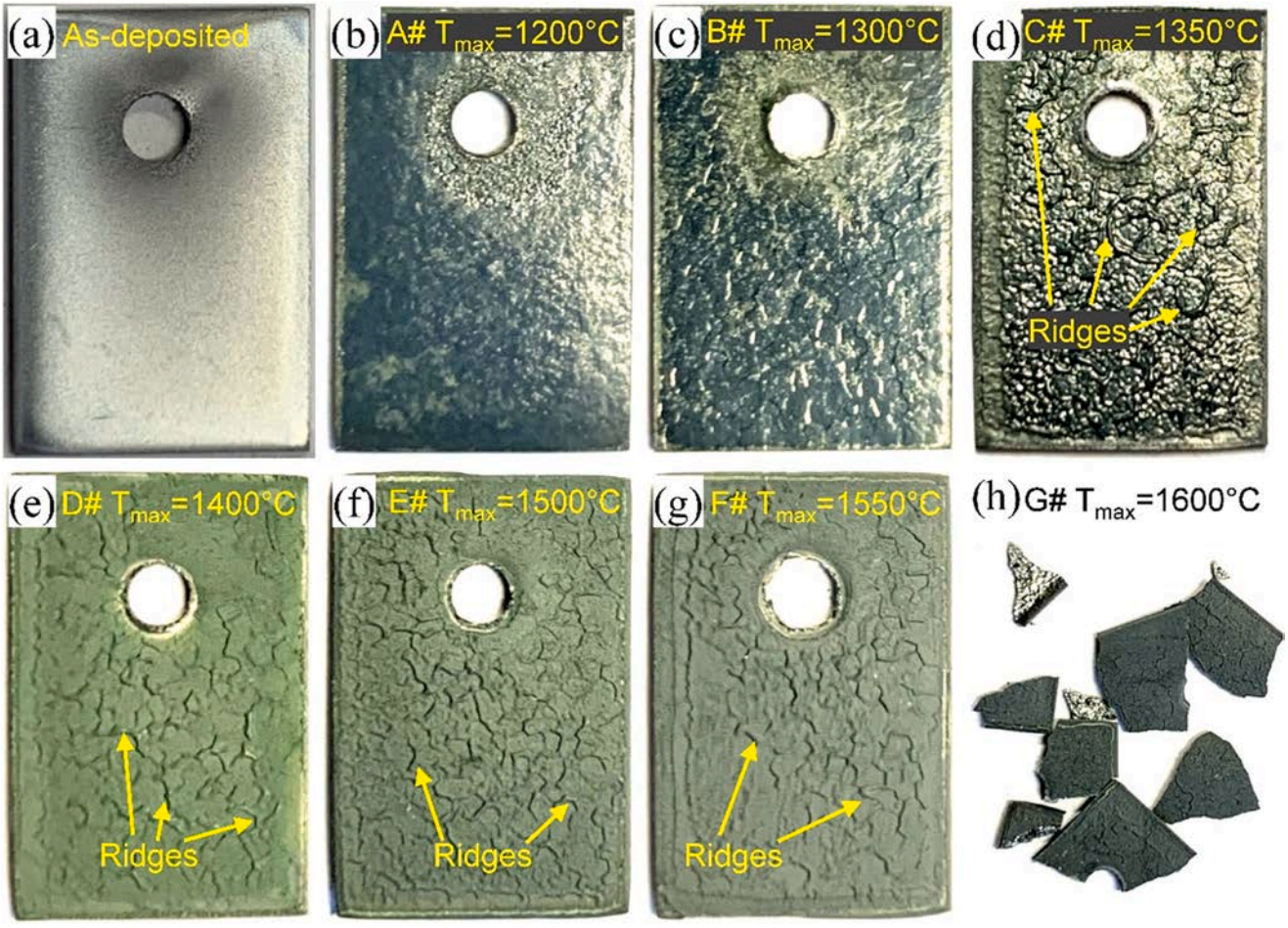

Fig. 5. Surface photos of the Cr-coated Zry-4 samples before and after oxidation.

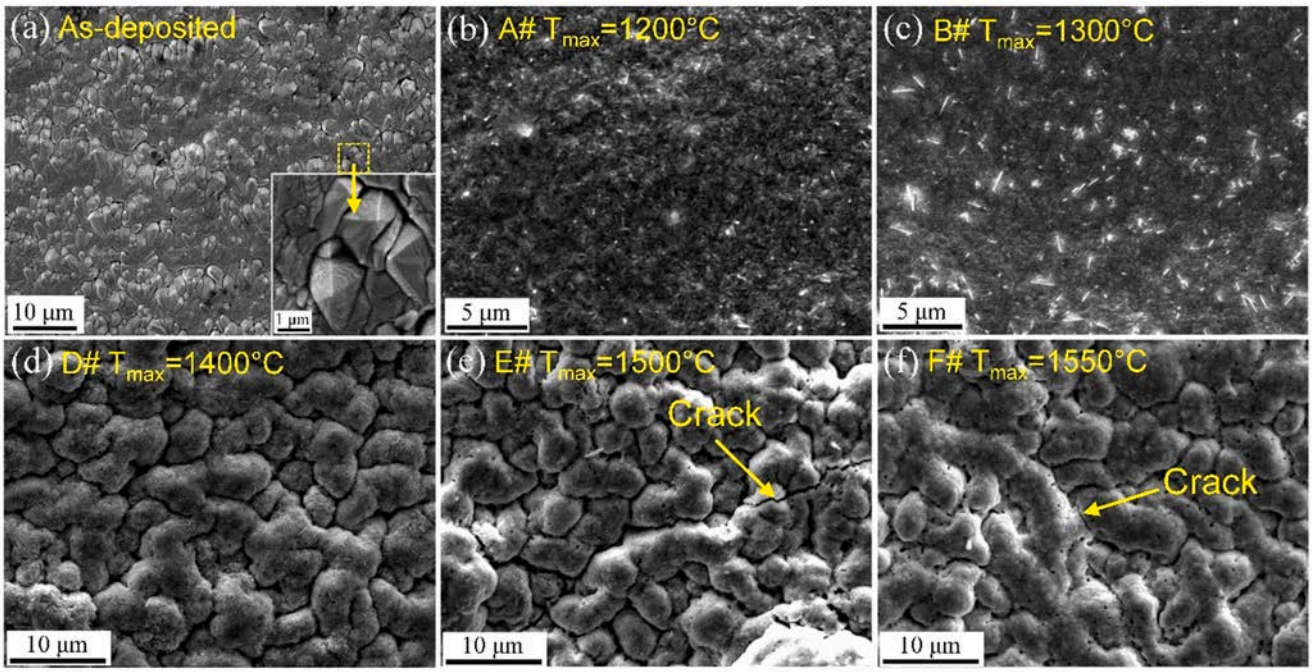

Fig. 6. Surface SEM images of the Cr-coated Zry-4 before and after transient steam oxidation.

for $T_{max} \geq 1400$ °C, the substrate is extensively attacked by steam and a thick zirconia layer forms beneath the coating (Fig. 7(d)–(i)). The zirconia grains are all in columnar shape at $T_{max} < 1550$ °C (Fig. 7(d) and (e)) and equiaxed grains appear beneath the columnar grains when the temperature climbs to 1550 °C (Fig. 7(f)) and 1600 °C (Fig. 7(i)). It is worth mentioning that there are cracks distributed along the grain boundaries of the equiaxed grains (Fig. 7 (i)).

3) **The α-Zr(O) layer in bulk grain**. An α-Zr(O) layer in bulk grain forms beneath the outer coating layer at T_{max} 1350 °C in the C# sample after oxidation (Fig. 7(c)). The thickness of the α-Zr(O) layer increases from ~70.1 μm in the C# sample (Fig. 7(c)) to ~132.8 μm in the D# sample (Fig. 7(d)) with temperature rising from 1350° to 1400 °C. Then the thickness decreases to ~39.6 μm in the E# sample (Fig. 7(e)) as temperature goes up to 1500 °C, eventually, this bulk grain α-Zr(O) layer disappears in the F# sample (Fig. 7(f)) when temperature rises to 1550 °C because most of the Zircaloy substrate is oxidized.
4) **The dual-phase (DP) layer**. A DP layer between the outer α-Zr(O) and the inner prior β-Zr is observed in the C# sample (T_{max} 1350 °C, Fig. 7(c)). Phases in this DP layer are identified as the Zr—Cr intermetallic compound phase and prior β-Zr phase by the back-scattered electron (BSE) SEM (Fig. 8(a)) and EDS maps (Fig. 8 (b)). Also Cr-rich segregation is observed at the interface between the α-Zr(O) layer and the DP layer while no Cr-rich precipitates distribute inside the central prior β-Zr substrate (Fig. 8(b)). When temperature rises to 1400 °C (Fig. 7(d)), at the central position of the substrate, the single prior β-Zr phase transforms into DP which is also identified as a combination of the Zr—Cr intermetallic compound and prior β-Zr phase by BSE SEM (Fig. 8(c)) and EDS maps (Fig. 8 (d)). Besides Cr, minimal Fe and Sn segregations are found in the central unoxidized substrate.
5) **The remaining metal**. There is unoxidized metal left even after oxidation at 1550 °C (Fig. 7(f)) and 1600 °C (Fig. 7(i)). Mainly two types of remaining metals are observed in the central region of the F# sample (Fig. 7(f)): single-phase along the equiaxed zirconia grain boundaries in Fig. 7(g) which was reported as the α-Zr(O) phase precipitated during the cooling stage [24,25] and multi-phase at the center in Fig. 7(h). The semi-quantitative elemental compositions in the remaining metal of the F# (Fig. 8(e)) and the G# samples (Fig. 8 (f)) were studied by EDS point analyses; the corresponding results are listed in Table 2. The inner equiaxed oxide phase at P1 of the F# sample is identified as nonstoichiometric ZrO_{2-x}. Three types of metal phases remain in the F# sample: 1) the Zr—Sn(O) phase at P2 position with Sn content up to ~29 at%; 2) the α-Zr(O) phase at P3 position with oxygen concentration ~30 at%; 3) the Zr—Cr(O) phase at P4 position with similar atomic contents of Zr and Cr. In the G# sample, only the Cr—Fe phase is observed at position P9. The equiaxed grain at P5 is also nonstoichiometric zirconia. The Cr_2O_3 phase (P7) distributes inside the ZrO_{2-x} layer. At the center of the sample, ZrO_{2-x} (P6) and Cr_2O_3 (p8) phases are detected which are the further oxidation products of α-Zr(O) and Zr—Cr(O). No α-Zr(O) phase or Zr—Cr(O) phase remained after oxidation.

3.4.2. The cross-sectional microstructures of the surface coating

Fig. 9 shows the cross-sectional SEM micrographs of the Cr coating before and after transient steam oxidation at different temperatures. As can be seen in Fig. 9(a), the as-deposited Cr coating with an average thickness of ~17.4 ± 1.1 μm is dense and well adherent to the Zry-4 substrate. At $T_{max} < 1400$ °C (Fig. 9(b)–(e)), the coating is all in a triple-layer structure with outer Cr_2O_3, middle unoxidized Cr, and inner Zr—Cr ($ZrCr_2$) phases according to the EDS maps of the B# sample in Fig. 9(d). This type of structure forming during the steam oxidation of the Cr coating was also observed and well discussed by other researchers [7,18,26]. Although the surface of the coating transforms from flat to fluctuant in C# sample at T_{max} 1350 °C (Fig. 9(e)), the structural integrity of the coating remains. In the B# sample (Fig. 9(d)), after steam oxidation at T_{max} 1300 °C, Cr-rich precipitates are observed inside the substrate, and inside the Cr coating there distribute Zr-rich precipitates, which were identified as ZrO_2 in former studies [7,26]. These ZrO_2 precipitates inside the Cr coating are more distinguishable in the C# sample (Fig. 9(e)). Therefore, to be more specific, the middle unoxidized Cr coating layer in the B# and C# samples should be a $Cr(ZrO_2)$ (Cr layer which contains ZrO_2) layer. When the temperature increases to 1400 °C (Fig. 9(f)), substrate oxidation occurs, and two types of coating structures are observed by EDS maps: one in Fig. 9(g) is similar with the

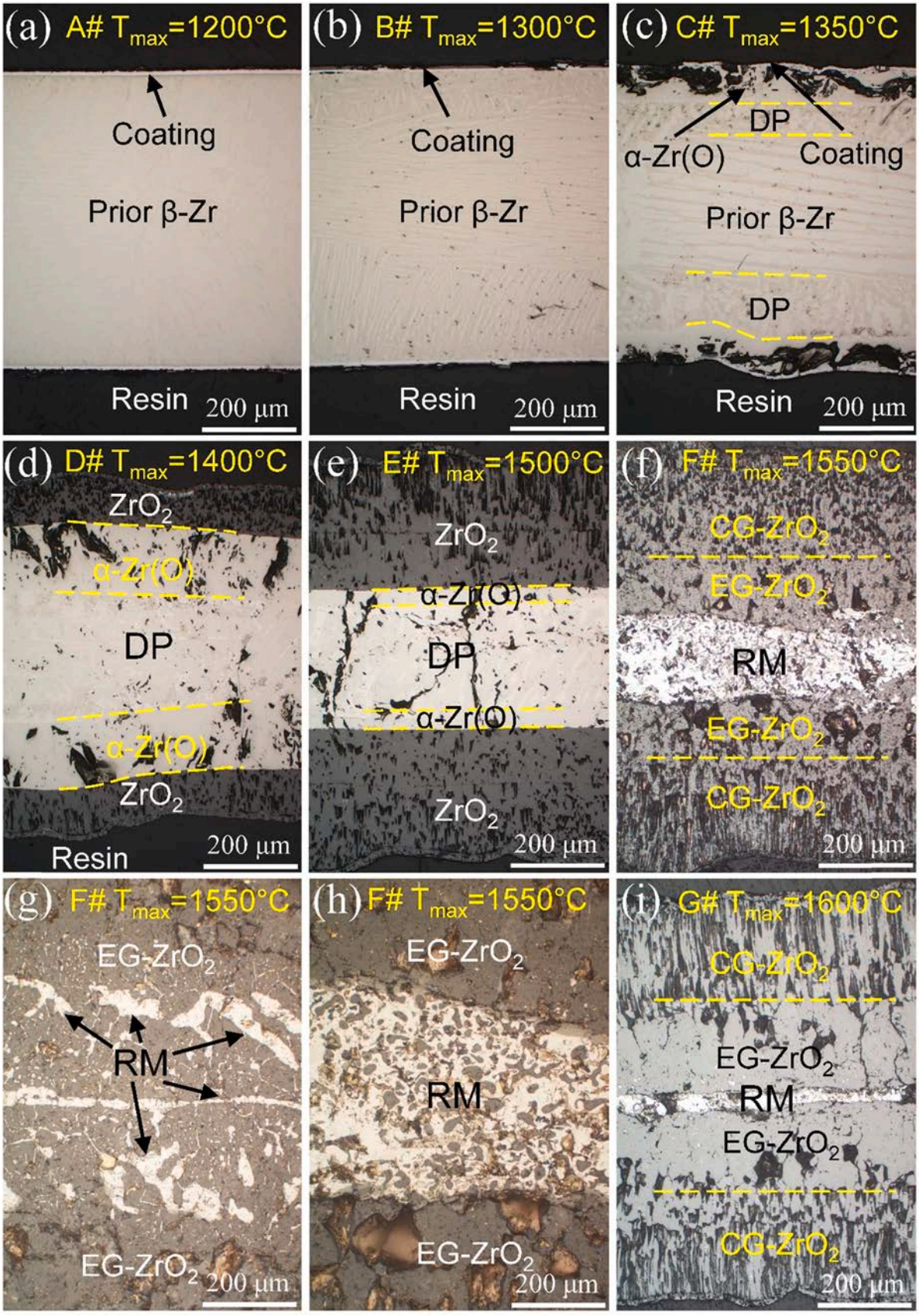

Fig. 7. The cross-sectional OM images of the Cr-coated Zry-4 before and after transient steam oxidation to different maximum temperature. T_{max} is the maximum temperature of the transient oxidation test; DP is Dual-phase; CG is Columnar grain; EG is Equiaxed grain; RM is Remaining metal.

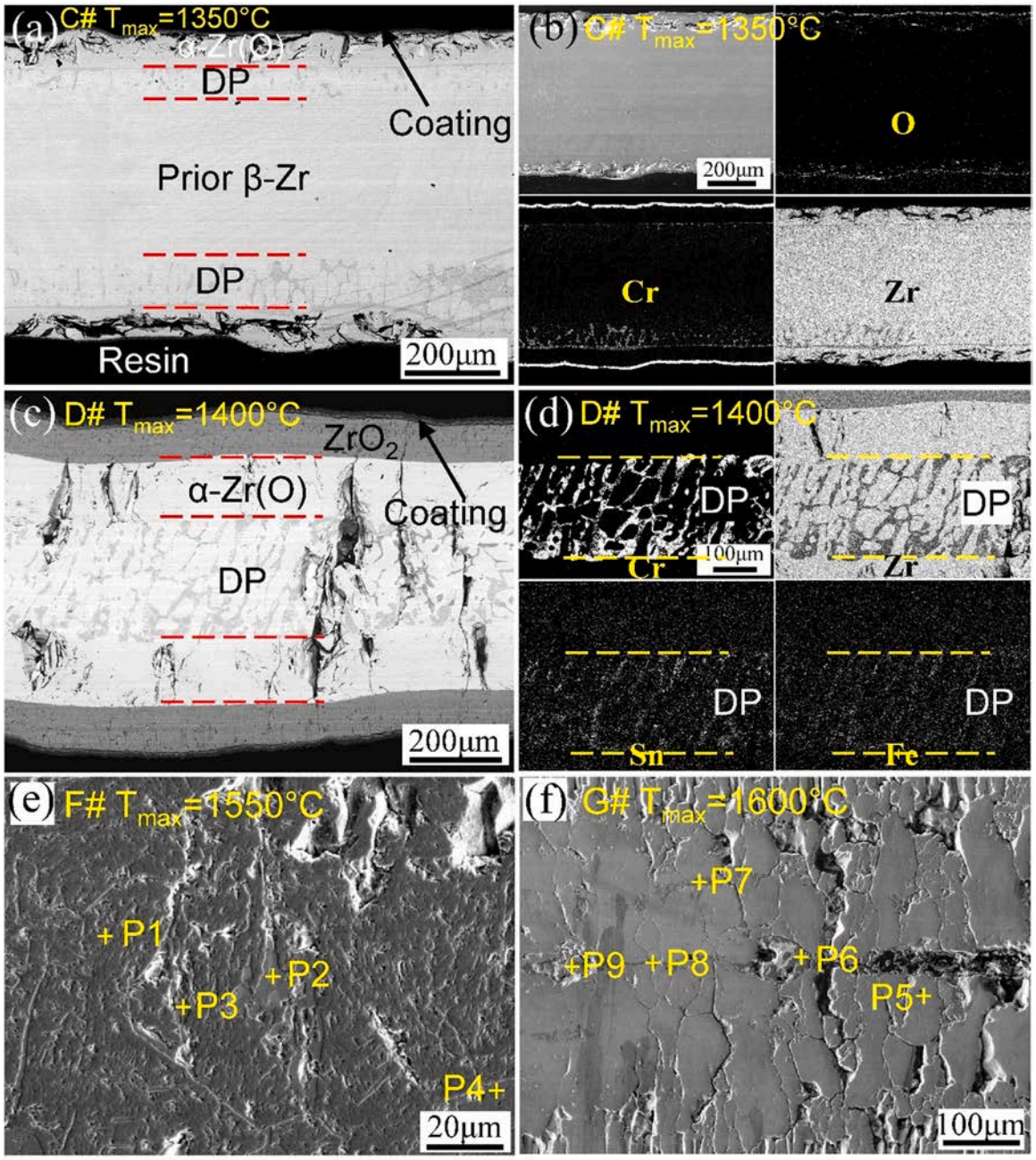

Fig. 8. The cross-sectional SEM images of the Cr-coated Zry-4 samples after transient steam oxidation: (a) BSE image of the C# sample; (b) EDS maps of the C# sample; (c) BSE image of the D# sample; (d) EDS maps of the D# sample; (e) SEM image of the center region in the F# sample; (f) SEM image of the center region in the G# sample.

Table 2
EDS point analyses about the semi-quantitative elemental contents of P1–P9 points in Fig. 8(e) and (f).

Atom (at%)	O	Cr	Fe	Zr	Sn
P1	57	0	0	43	0
P2	18	0	0	53	29
P3	30	0	0	68	2
P4	13	43	2	42	0
P5	63	0	0	37	0
P6	63	4	0	33	0
P7	62	37	0	1	0
P8	59	37	2	2	0
P9	15	75	9	0	1

structure in the B# sample (Fig. 9(d)). However, instead of the Zr—Cr layer, a ZrO_2(Cr) layer appears between the coating and substrate, also the thickness of the outer Cr_2O_3 scale in the D# sample is thinner than that in the B# and C# samples. The other is also a triple-layer structure with outer Cr_2O_3(ZrO_2) layer, middle ZrO_2(Cr_2O_3) layer, and inner Cr_2O_3 layer which can be seen in BSE SEM (Fig. 9(f)) and EDS maps (Fig. 9(h)). In both types of coating structures, ZrO_2 grains form along the grain boundaries of Cr. These ZrO_2 grains connect the substrate and the atmosphere, and can act as oxygen diffusion paths during the steam oxidation. At $T_{max} \geq 1500$ °C (E# in Fig. 9(i), F#, and G# samples), the coating layer sequence keeps similar with that of the D# sample in Fig. 9 (f). Large cracks can be found inside the coatings.

The thickness evolution of the whole coating and each sublayer in different samples is summarized in Fig. 10. The data of the D# sample

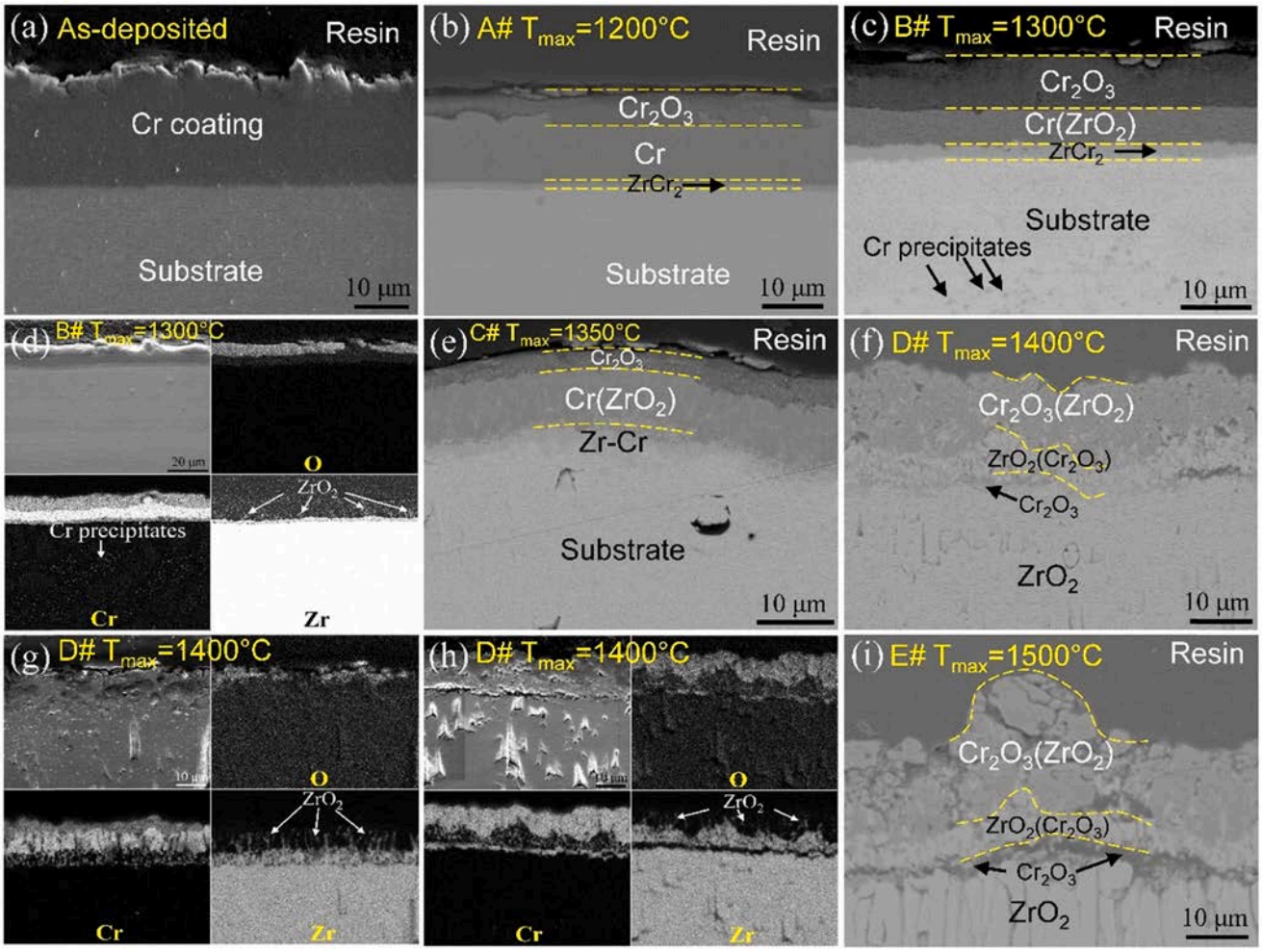

Fig. 9. The cross-sectional SEM images of the Cr-coated Zry-4 (a) before transient steam oxidation, and after transient steam oxidation: (b) A# sample; (c) B# sample; (d) EDS maps of the B# sample; (e) C# sample; (f) D# sample; (g) and (h) EDS maps of the D# sample with different coating structure; (i) E# sample.

used here is the mixed-oxide structure in Fig. 9(f). The error bars of the A#, B#, and C# samples are measurement errors of the total thickness of the coatings. As can be seen in Fig. 10, the total thickness of the coating decreases from originally 17.4 ± 1.1 μm in the as-deposited sample to a thinnest 12.5 ± 0.8 μm in the C# sample with T_{max} 1350 °C. It is worth mentioning that the actual coating thickness decrease should be larger than the value in Fig. 10 because of the large Pilling-Bedworth ratio (PBR) of Cr_2O_3 (~2) [27] which can lead to volume expansion and thickness increase during the oxidation of Cr. The total thickness of the coating grows to 18.3 ± 1.4 μm in the D# sample, which is larger than the original coating thickness when the temperature rises to 1400 °C. The coating thickness fluctuates with the further increase of temperature due to the measurement error. The thickness of the outer dense Cr_2O_3 scale first increases from ~4.7 μm in the A# sample to ~7.5 μm in the B# sample when temperature rises from 1200 °C to 1300 °C, then abruptly decreases to ~3.0 μm in the C# sample with further increase of temperature to 1350 °C. The thickness evolution of the $Cr/Cr(ZrO_2)$ (Cr or $Cr(ZrO_2)$) layer has an opposite trend than the Cr_2O_3 layer. The thickness of the Zr—Cr layer increases from ~1.3 μm in the A# sample to ~2.0 μm in the B# sample and then does not change too much in the C# sample.

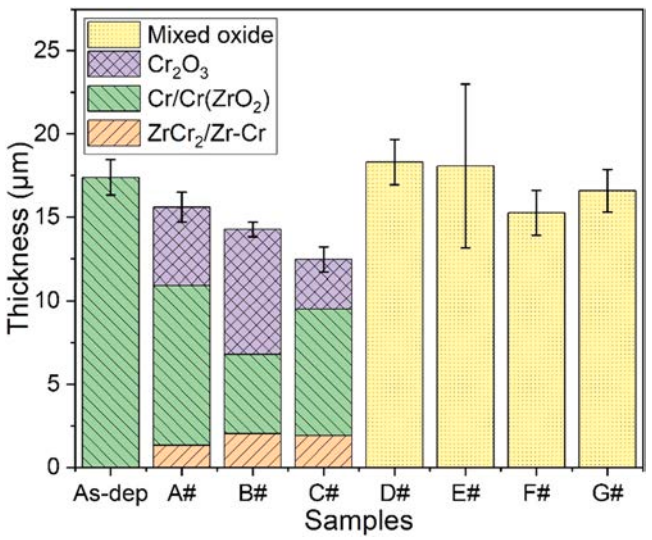

Fig. 10. Thickness evolution of the coating and each sublayer of all samples.

4. Discussion

4.1. The oxidation behavior and microstructural evolution of the Cr coating

Fig. 11 shows a schematic that illustrates the microstructural evolution of the Cr coating layer during the transient steam oxidation. At the beginning of the steam oxidation (Fig. 11(b)), the reaction between Cr

coating and steam leads to the formation of the single-phase dense Cr_2O_3 scale on the outer surface of coating [14,28]. The reaction can be given by:

$$2Cr + 3H_2O \rightarrow Cr_2O_3 + 3H_2 \quad (1)$$

The oxidation of chromium is dominated by the outward diffusion of chromium cations through the oxide layer (Fig. 11(b)). The new oxide grains are produced at the gas/oxide interface, which has been extensively investigated in other studies [14,29–32]. At the same time, a small amount of oxygen diffuses inward to the inner coating and substrate via grain boundaries, and this part of oxygen mainly is dissolved in the Cr coating [19] or gets absorbed by the substrate and forms an α-Zr(O) layer between the coating and prior β-Zr substrate (Fig. 7). At high temperature, a solid-state reaction between the Cr coating and Zr substrate occurs owing to the interdiffusion of Zr—Cr system [19,33]. An intermetallic compound layer forms between the Cr coating and Zr substrate. The reaction can be given by:

$$Zr + 2Cr \rightarrow ZrCr_2 \quad (2)$$

This layer was also identified as $Zr(Cr, Fe)_2$ laves phase if there is Fe in the substrate [7,14,34,35]. Except for the formation of the $ZrCr_2$ layer, the inward diffused Cr also dissolves in the Zr substrate due to its large diffusion coefficient and high solubility in β-Zr [7,14,19], which results in further thickness decrease of the coating (Fig. 10) [19]. With the increase of temperature to 1300 °C (Fig. 11(c)), the oxidation rate of the Cr coating, the Zr—Cr interdiffusion rate, and the Zr—Cr solid-state reaction rate intensify. As a result, a thicker oxide scale and a thicker $ZrCr_2$ layer form while the thickness of the unoxidized Cr coating and the whole thickness of the coating further decrease. At this temperature, the outward diffused Zr is oxidized on the Cr grain boundaries by the dissolved and inward diffused oxygen [7] due to the higher oxygen affinity of Zr than Cr (the standard Gibbs formation energies per mole of O_2 of ZrO_2 and Cr_2O_3 are 858 and 538 kJ/mol at 1000 °C, respectively [36]). It is worth mentioning that the grain boundary diffusion rate of Cr, Zr, and O at this temperature should be much larger than the volume diffusion rate, and it is the reason why Zr diffuses outward and is oxidized on the grain boundaries of Cr. Therefore, the unoxidized Cr layer transforms to a $Cr(ZrO_2)$ layer confirmed by the appearance of ZrO_2 precipitates along the Cr grain boundaries.

When temperature reaches 1350 °C (Fig. 11(d)), the thickness of the outer dense Cr_2O_3 scale significantly decreases while the thickness of the $Cr(ZrO_2)$ layer increases to some extent (Fig. 10). This phenomenon was also observed by Han et al. [4,6]. In their studies, a reaction between Zr and Cr_2O_3 as given in Eq. 3 was proposed resulting in the reduction of the outer dense Cr_2O_3 to Cr metal at high temperature and the formation of a ZrO_2 layer beneath the coating.

$$3Zr + 2Cr_2O_3 \rightarrow 4Cr + 3ZrO_2 \quad (3)$$

This reaction provides an explanation for the thickening of the unoxidized Cr coating layer and the thinning of the outer dense oxide scale. The reduction of Cr_2O_3 can be one factor that results in the thickness decrease of the dense Cr_2O_3 scale in the current experiments, however, there should be other reasons that cause the consumption of Cr_2O_3. On the one hand, in the current experiments, no continuous ZrO_2 layer forms beneath the unoxidized Cr coating at 1350 °C. The formation mechanism of the ZrO_2 grains on the Cr grain boundaries was

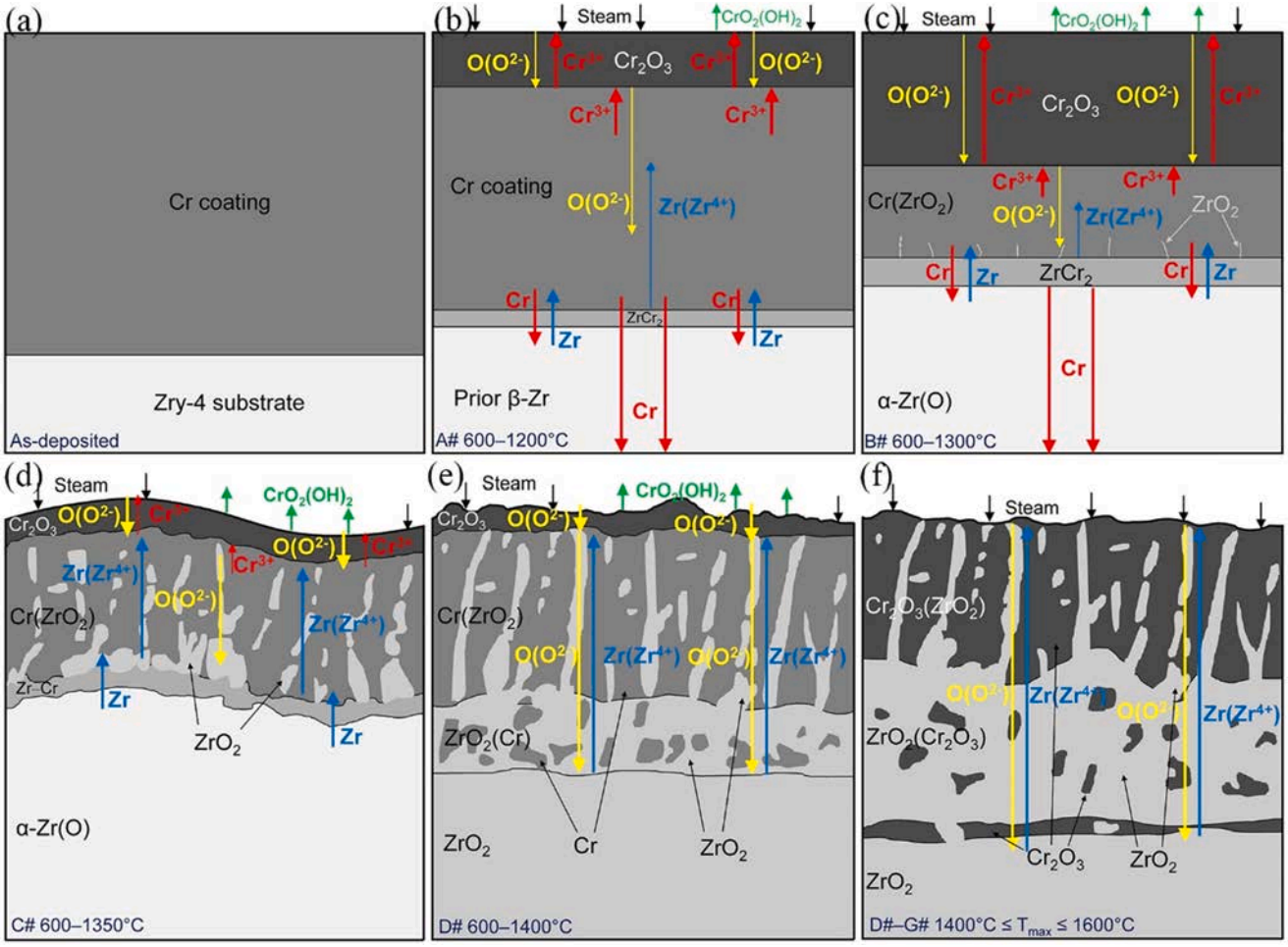

Fig. 11. Schematic of the microstructural evolution of the surface Cr coating during transient steam oxidation.

suggested as the reaction between the inward diffused oxygen and the outward diffused Zr [7] rather than the direct reaction between Zr and Cr_2O_3. On the other hand, the thickness increase of the unoxidized Cr coating layer in the current experiments is mainly caused by the outward diffusion and oxidation of Zr, which lead to a volume expansion due to the large PBR of the oxidation reaction (1.56 [37]). The volume ratio between the ZrO_2 precipitates and the unoxidized Cr is ~32% (deviation: −10% to +20%) calculated by the Image-Pro Plus software through the color difference between ZrO_2 and Cr using the BSE SEM image in Fig. 9(e). This result indicates that the formation of the ZrO_2 precipitates leads to a 32% increase in the thickness of the unoxidized Cr coating. Because in this experiment, the volume expansion of coating can be possibly considered as 1-D expansion along the coating thickness direction for the following reasons: 1) there is no constraint on the outside of the coating to inhibit the free expansion of the coating along the coating thickness direction; 2) the expansion of the coating in the direction parallel to the coating/substrate interface can be inhibited by the adhesion force between the coating and substrate; and 3) the expansion of the coating in local regions along the direction parallel to the coating/substrate interface can be inhibited by the coating in the adjacent regions. This value is close to the actual thickness increase in percentage (46% ± 10%) of the $Cr(ZrO_2)$ layer in the C# sample relative to that in the B# sample calculated by the thickness data in Fig. 10. This ZrO_2-caused thickness growth can also be confirmed by the total coating thickness increase of the D#–G# samples (Fig. 10) in which lots of ZrO_2 precipitates form inside the coating and lead to the significant thickness increase of the coating.

At such a high temperature, the volatilization of the oxide layer may be another reason for the thinning of the oxide layer, even though previous studies [7,38] suggested that the volatilization rate of Cr_2O_3 is too small to consider its effects on oxidation kinetics and coating microstructure at a relatively low temperature. Besides, Yeom et al. [14] suggested that the volatilization of Cr_2O_3 in steam led to a quartic oxidation kinetics of the cold spray Cr coatings at 1230 °C and above. During the high temperature oxidation of other Cr-containing alloys such as 304L [39] and 310S [40] stainless steels, the evaporation of Cr_2O_3 could cause the dense protective oxide layer failure and breakaway oxidation. However, a systematic investigation of the thickness decrease behavior and mechanism should be conducted in the future.

For T > 1332 °C, the Zr—Cr eutectic reaction occurs at two positions: one is in the Zr—Cr layer at the coating/substrate interface; and the other is inside the prior β-Zr substrate due to the inward diffusion of Cr from the coating to substrate. The microstructure and structural integrity of the coating could be affected by the Zr—Cr eutectic reaction, which leads to the structural transformation of coating surface from flat to corrugated and the appearance of ridges on the surface through the formation of a liquid phase. The eutectic reaction inside the prior β-Zr substrate should be dominant for the structural transformation of coating, because the thickness of the dual phase layer beneath the α-Zr (O) is far higher than that of the Cr—Zr layer between the Cr coating and the α-Zr(O). During the structural transformation, deformation occurs inside the coating. Due to the low ductility of the Cr_2O_3 scale, microcracks can be generated inside the coating when eutectic reactions occur. The main reason for the rapid oxidation at 1350 °C is the failure of the protective coating, which is specifically reflected by the thinning of the dense Cr_2O_3 layer and the coating deformation in the current experiments. A lot of oxygen diffuses into the coating through the remaining thin oxide layer and reacts with the Zr, which diffuses outward from the substrate to the coating. This oxidation reaction produces ZrO_2 on Cr grain boundaries. These ZrO_2 grains enlarge the diffusion of oxygen into the substrate [7] and destroy the structural integrity of the unoxidized Cr coating, resulting in the formation of the α-Zr(O) layer at 1350 °C. It is worth mentioning that the higher oxygen affinity of Zr than Cr leads to the preferential oxidation of Zr and inhibits the oxidation of the remaining Cr metal in the coating.

With the gradual thickness decrease of the outer single-phase dense Cr_2O_3 layer (Fig. 11(e)) and increase of the inward diffusion of oxygen, the Zr—Cr layer and α-Zr(O) substrate are oxidized into ZrO_2. A Cr metal layer is left at the original position of the Cr—Zr layer following Eq. 4:

$$ZrCr_2 + 2O \rightarrow ZrO_2 + 2Cr \quad (4)$$

As shown in Fig. 11(f), when the outer single-phase dense protective Cr_2O_3 layer (here the single-phase Cr_2O_3 layer just indicates the outermost Cr_2O_3 scale in Fig. 11(b)–(e), but does not include the Cr_2O_3 inside the non-protective $Cr_2O_3(ZrO_2)$ layer in Fig. 11(f)) totally disappears and the oxidation rate of the substrate gradually decreases with the growth of a dense columnar ZrO_2 layer, the Cr metal in the $Cr(ZrO_2)$ layer and at the coating/substrate interface are oxidized into Cr_2O_3. Hence, the coating completely loses its protective effect and the coating microstructure almost keeps similar with that of the D# sample even the temperature increases to 1600 °C.

4.2. The microstructural evolution and oxidation behavior of the Zry-4 substrate

Fig. 12 depicts the microstructural evolution schematic of the Zry-4 substrate during the transient steam oxidation. The Zry-4 substrate transforms from α-Zr (Fig. 12(a)) to β-Zr (Fig. 12(b)) at T > 865 °C [41]. Due to the high oxygen affinity of Zr, an oxygen stabilized α-Zr(O) bulk grain layer forms beneath the coating during the steam oxidation for T_{max} 1350 °C by absorbing the oxygen which dissolves in the Cr coating and diffuses from the outer coating surface through the grain boundaries of the dense Cr_2O_3 scale and the unoxidized Cr coating [7]. Cr diffuses inward and dissolves in the Zry-4 substrate (mainly in β-Zr) [19]. With the concentration increase of Cr in the substrate, Cr-rich precipitates form inside the β-Zr during the cooling stage (Fig. 12(b)) [14,19]. The inward diffusion of Cr from the coating to the substrate is mainly ceased at 1350 °C when there is a thick α-Zr(O) layer in the bulk forms between the coating and prior β-Zr (Fig. 12(c)). It is noteworthy that the α-Zr(O) layer grows rapidly at temperature from 1350 °C (sample C#) to 1400 °C (sample D#), which indicates the inward diffusion of O into β-Zr and the transformation of β-Zr to α-Zr(O) when the oxygen concentration reaches its solubility limit in β-Zr. So at the growth front of the α-Zr(O) layer, the transformation of β-Zr to α-Zr(O) occurs all the time. Therefore, a Cr-rich layer precipitates at the growth front of the α-Zr(O) (which is the interface between α-Zr(O) and β-Zr) due to the low solid solubility of Cr in α-Zr(O) [19]. The formation of the DP layer between the α-Zr(O) layer and prior β-Zr (Fig. 12(c)) is due to the precipitation of β-Zr and the solidification of the residual eutectic phase when the temperature decreases below 1332 °C during the cooling stage [7].

For 1350 °C < T < 1400 °C (Fig. 12(d)), the coating loses its protective effect and substantial amount of oxygen diffuses into the substrate. The α-Zr(O) layer is oxidized into t-ZrO_{2-x} and the inner β-Zr continuously transforms to α-Zr(O) with the inward diffusion of oxygen. The Cr that dissolved in β-Zr gradually diffuses inward and concentrates at the sample center. The Zr—Cr eutectic reaction then occurs at the central substrate and the DP structure forms when the sample is cooled down. In addition, the alloying elements such as Sn and Fe, which have a lower oxygen affinity than Zr, diffuse to the central position during the oxidation of the substrate. This kind of columnar dense t-ZrO_{2-x} growth, Zr substrate consumption, and inward diffusion of Cr continues until temperature rises to 1500 °C. Then a crystal transformation from columnar to equiaxed ZrO_{2-x} occurs between 1500 and 1550 °C and the zirconia layer turns into a bilayer structure with outer columnar and inner equiaxed grains as shown in Fig. 12(f). The columnar to equiaxed transformation is caused by the reaction between t-ZrO_{2-x} and α-Zr(O) and the formation of c-ZrO_{2-y} in the following Eq. 5 [42]. Because of the different oxygen vacancy concentrations in tetragonal and cubic zirconia phases, here different symbols x and y were used.

$$\alpha\text{-}Zr + t\text{-}ZrO_{2-x} \rightleftharpoons c\text{-}ZrO_{2-y} (x < y) \quad (5)$$

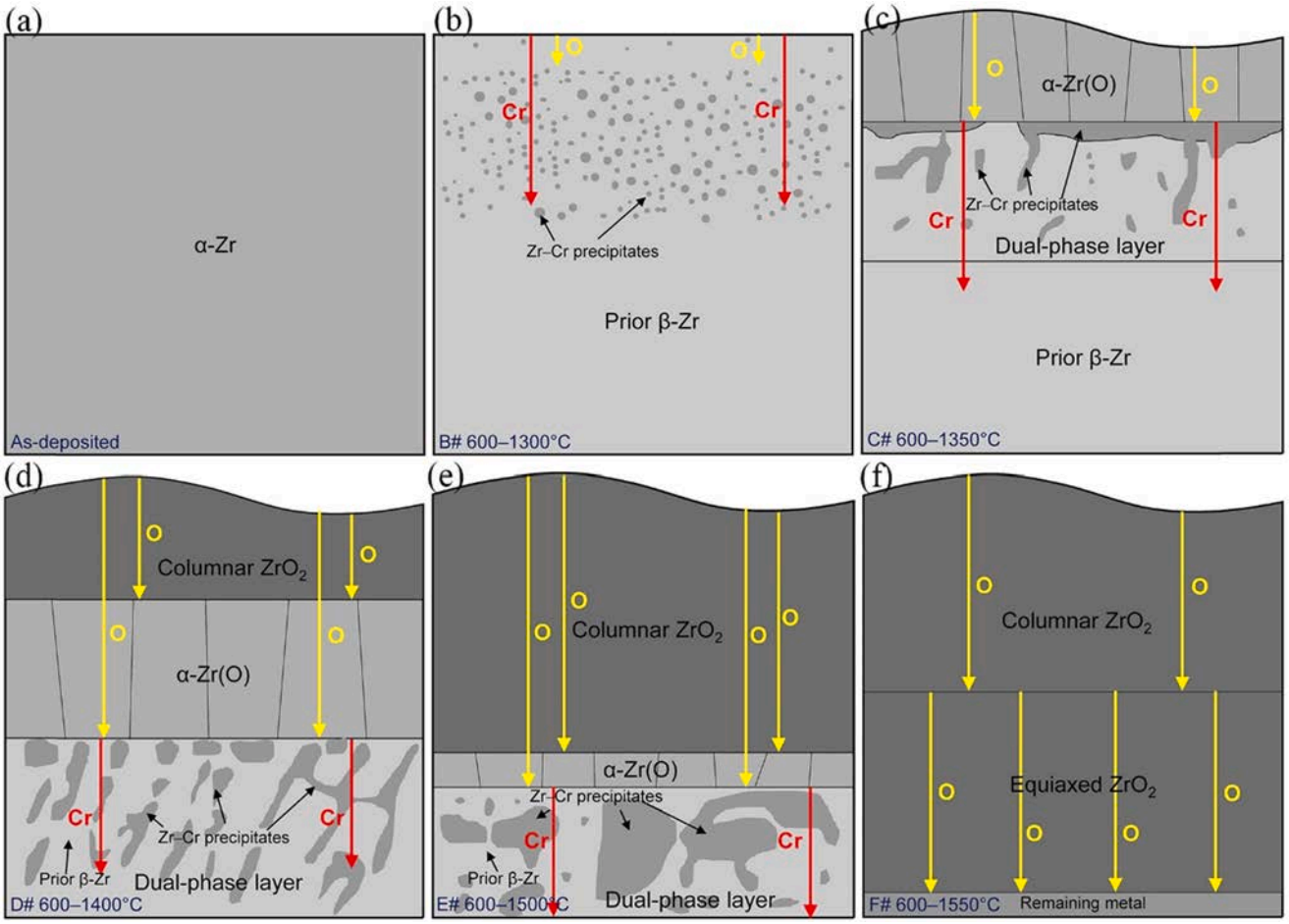

Fig. 12. Schematic of the microstructural evolution of the Zircaloy substrate during transient steam oxidation.

This transformation of t-ZrO_{2-x} to c-ZrO_{2-y} occurs at ~1525 °C at normal pressure [42]. The phase-transition temperature could be decreased by large compressive stress, which can stabilize the metastable phase inside the ZrO_{2-y} layer [43]. In addition, the impurity elements in ZrO_{2-x} can affect the phase-transition temperature [43]. The transformation of t-ZrO_{2-x} to c-ZrO_{2-y} accelerates the oxidation process of the remaining Zr and other remaining metals at the substrate center owing to the larger oxygen lattice diffusion coefficient in c-ZrO_{2-y} phase [44,45] and the formation of cracks along the grain boundaries of the equiaxed c-ZrO_{2-y} layer (Fig. 8(f)). During the cooling stage, the decomposition of c-ZrO_{2-y} in Eq. 6 [42] occurs and α-Zr(O) phase segregates on the grain boundaries of the equiaxed ZrO_{2-x} (Fig. 7(g)) [24].

$$\text{c}\quad ZrO_{2\ y} \rightleftharpoons \alpha\quad Zr + \text{t}\quad ZrO_{2\ x} (x < y) \tag{6}$$

At the center of the samples, there should be eutectic phases between Zr, Cr, Fe, and Sn formed at 1550 °C, and mainly three types of phases recrystallize during the cooling stage: α-Zr(O), Zr—Cr(O), and Zr—Sn(O) phases. Theoretically, the remaining Cr, Sn, and Fe are oxidized only after the Zr is consumed, which can be seen in the G# sample. After oxidation at 1600 °C, no α-Zr(O) phase is observed while Cr and Fe are not totally oxidized. Therefore, when the sample fractured into pieces, the fast oxidation of the central metal leads to a sharp hydrogen release peak.

4.3. Summary of the five stages of Cr-coated Zircaloy oxidation behavior

After the analyses and discussions about the microstructural evolution of the surface coating and substrate, the degradation mechanisms of the Cr coating correlating with the hydrogen release in each stage can be clearly defined:

1) **Stage I**: The oxidation of the Cr coating and the formation of a protective dense Cr_2O_3 scale follows Eq. 1. Interdiffusion between Cr coating and Zr substrate.
2) **Stage II**: The dense structure of the outer protective Cr_2O_3 scale is destroyed by the reaction between Zr and Cr_2O_3 following Eq. 3, the Zr—Cr eutectic reaction, and potentially the volatilization of Cr_2O_3. Furthermore, the outward diffusion and oxidation of Zr along grain boundaries in the unoxidized Cr coating provides oxygen diffusion paths. Eventually, coating failure occurs and oxygen diffuses massively into the substrate causing extensive oxidation.
3) **Stage III**: With the extensive oxidation of the Zr substrate, a dense columnar oxide layer forms and acts as an oxygen diffusion barrier, which could effectively decrease the oxidation rate and reduce the hydrogen release.
4) **Stage IV**: The transformation of t-ZrO_{2-x} to c-ZrO_{2-y} leads to the transition of dense columnar grains to bulk equiaxed grains with cracks and an increased oxygen diffusion coefficient in the zirconia layer. Consequently, the release of hydrogen is accelerated.
5) **Stage V**: The oxidation of the remaining inward diffused Cr, Fe, and Sn whose oxygen affinity is much lower compared to Zr, so the oxidation rate and hydrogen release rate decrease gradually. The appearance of the third peak is mainly caused by the fracture of the sample and the exposure of the remaining metals to steam.

5. Conclusion

The transient steam oxidation behavior of Zry-4 sheet samples with

~17.4 μm-thick Cr coating deposited using a magnetron sputtering method was comprehensively investigated in transient tests from 600 °C to a temperature between 1200 and 1600 °C with a low heating rate of 10 K/min. The surface Cr coating on Zry-4 significantly improved the steam oxidation resistance of the substrate and reduced the total hydrogen release up to 1500 °C. However, the oxidation rate of the coated samples exceeded the non-coated ones from approx. 1350 °C. The microstructures of the samples after steam oxidation were examined in depth. The transient steam oxidation behavior and the hydrogen release kinetics during the oxidation of the Cr-coated Zry-4 at temperature from 600 °C to 1600 °C can be divided into five stages, which correlates to the microstructural evolution of the surface coating and substrate. The current results were obtained at a low heating rate of 10 K/min, so the data obtained in this work cannot be directly extrapolated to design-basis accident and beyond design-basis accident scenarios, which have faster heating rates. The effect of heating rate on the transient steam oxidation behavior of Cr-coated Zircaloy needs to be further investigated. Several crucial conclusions are drawn from the obtained results:

(1) A single-phase dense Cr_2O_3 scale forms on the outer surface of the Cr coating by the reaction between Cr and steam. The thickness of this Cr_2O_3 scale first increases by oxidation then decreases through the reduction of Cr_2O_3 by Zr and possibly, at higher temperatures, the volatilization of Cr_2O_3 in steam. The single-phase protective oxide scale finally disappears but instead, a new non-protective $Cr_2O_3(ZrO_2)$ layer forms.
(2) Zr diffuses outward from the substrate to the Cr coating layer along the Cr grain boundaries, is oxidized by the inward diffusing oxygen, and forms ZrO_2 precipitates which provide oxygen diffusion paths. When the outer single-phase dense protective Cr_2O_3 scale completely disappears, ZrO_2 grains connected the outer coating surface and substrate and eventually impact the structural integrity of the unoxidized Cr coating.
(3) Cr diffuses into the bulk at high temperature, which leads to the coating thickness decrease. Zr—Cr eutectic reaction occurs at the coating/substrate interface and inside the substrate when the temperature is higher than 1332 °C. The eutectic reaction results in the fluctuant surface and affects the coating microstructure. Cr gradually diffused to the center of the substrate, and is finally oxidized.
(4) The coating failure behavior is due to the combined effects of the oxidation of Cr, the inward diffusion of Cr into the substrate, the reduction of the Cr_2O_3 scale by Zr, the formation of ZrO_2 precipitates along the grain boundaries of Cr, the Zr—Cr eutectic reaction, and possibly the volatilization of the Cr_2O_3 scale.
(5) Independently from the coating, the transformation of t-ZrO_{2-x} to c-ZrO_{2-y} ($y > x$) at approx. 1500 °C increases the oxygen diffusion coefficient due to the high vacancy concentration in c-ZrO_{2-y}. The phase transformation further leads to the transition of dense columnar grains to loose equiaxed grains with increasing oxidation rate.
(6) Sn and Fe diffuse inward to the center of the substrate during the consumption of the substrate and are finally oxidized.

CRediT authorship contribution statement

Junkai Liu: Conceptualization, Methodology, Investigation, Writing – original draft. **Chongchong Tang:** Investigation, Methodology, Writing – review & editing. **Martin Steinbrück:** Conceptualization, Project administration, Writing – review & editing. **Jianqiao Yang:** Resources. **Ulrike Stegmaier:** Investigation, Writing – review & editing. **Mirco Große:** Conceptualization, Writing – review & editing. **Di Yun:** Supervision. **Hans Jürgen Seifert:** Supervision.

Declaration of Competing Interest

The authors declare that they have no known competing financial interests or personal relationships that could have appeared to influence the work reported in this paper.

Data availability

The raw data required to reproduce these findings cannot be shared at this time as the data also forms part of an ongoing study. The processed data required to reproduce these findings cannot be shared at this time as the data also forms part of an ongoing study.

Acknowledgments

Junkai Liu is supported by the China Scholarship Council, China (No. 201906280379). The work was conducted in the framework of the HGF program NUSAFE in Karlsruher Institut für Technologie, Germany.

References

[1] J.K. Liu, X.H. Zhang, D. Yun, A complete review and a prospect on the candidate materials for accident-tolerant fuel claddings, Mater. Rev. 32 (2018) 1757–1778.
[2] C. Tang, M. Stueber, H.J. Seifert, M. Steinbrueck, Protective coatings on zirconium-based alloys as accident-tolerant fuel (ATF) claddings, Corros. Rev. 35 (2017) 141–165.
[3] K.A. Terrani, Accident tolerant fuel cladding development: promise, status, and challenges, J. Nucl. Mater. 501 (2018) 13–30.
[4] X. Han, Y. Wang, S. Peng, H. Zhang, Oxidation behavior of FeCrAl coated Zry-4 under high temperature steam environment, Corros. Sci. 149 (2019) 45–53.
[5] D. Jin, N. Ni, Y. Guo, Z. Zou, X. Wang, F. Guo, X. Zhao, P. Xiao, Corrosion of the bonding at FeCrAl/Zr alloy interfaces in steam, J. Nucl. Mater. 508 (2018) 411–422.
[6] X. Han, J. Xue, S. Peng, H. Zhang, An interesting oxidation phenomenon of Cr coatings on Zry-4 substrates in high temperature steam environment, Corros. Sci. 156 (2019) 117–124.
[7] J. Brachet, E. Rouesne, J. Ribis, T. Guilbert, S. Urvoy, G. Nony, C. Toffolon-Masclet, M. Le Saux, N. Chaabane, H. Palancher, A. David, J. Bischoff, J. Augereau, E. Pouillier, High temperature steam oxidation of chromium-coated zirconium-based alloys: kinetics and process, Corros. Sci. 167 (2020), 108537.
[8] G. Li, C. Cai, Y. Wang, Y. Zhou, L. Yang, J. Lu, G. Zhou, Zirconium silicate growth induced by the thermochemical interaction of yttria-stablized zirconia coatings with molten CMAS deposits, Corros. Sci. 149 (2019) 249–256.
[9] Y.J. Park, J.W. Kim, G. Ali, S.O. Cho, Enhancement of oxidation resistance of zirconium alloy with anodic nanoporous oxide layer in high-temperature air/steam environments, Corros. Sci. 140 (2018) 217–222.
[10] J. Liu, Z. Hao, Z. Cui, D. Ma, J. Lu, Y. Cui, C. Li, W. Liu, S. Xie, P. Hu, P. Huang, G. Bai, D. Yun, Oxidation behavior, thermal stability, and the coating/substrate interface evolution of CrN-coated Zircaloy under high-temperature steam, Corros. Sci. 185 (2021), 109416.
[11] J. Liu, Z. Cui, D. Ma, J. Lu, Y. Cui, C. Li, W. Liu, Z. Hao, P. Hu, M. Yao, P. Huang, G. Bai, D. Yun, Investigation of oxidation behaviors of coated Zircaloy as accident-tolerant fuel with CrAlN and CrAlSiN coatings in high-temperature steam, Corros. Sci. 175 (2020), 108896.
[12] C. Tang, M. Steinbrueck, M. Stueber, M. Grosse, X. Yu, S. Ulrich, H.J. Seifert, Deposition, characterization and high-temperature steam oxidation behavior of single-phase Ti 2 AlC-coated Zircaloy-4, Corros. Sci. 135 (2018) 87–98.
[13] J.G. Gigax, M. Kennas, H. Kim, T. Wang, B.R. Maier, H. Yeom, G.O. Johnson, K. Sridharan, L. Shao, Radiation response of Ti2AlC MAX phase coated Zircaloy-4 for accident tolerant fuel cladding, J. Nucl. Mater. 523 (2019) 26–32.
[14] H. Yeom, B. Maier, G. Johnson, T. Dabney, M. Lenling, K. Sridharan, High temperature oxidation and microstructural evolution of cold spray chromium coatings on Zircaloy-4 in steam environments, J. Nucl. Mater. 526 (2019), 151737.
[15] T. Wei, R. Zhang, H. Yang, H. Liu, S. Qiu, Y. Wang, P. Du, K. He, X. Hu, C. Dong, Microstructure, corrosion resistance and oxidation behavior of Cr-coatings on Zircaloy-4 prepared by vacuum arc plasma deposition, Corros. Sci. 158 (2019), 108077.
[16] E.B. Kashkarov, D.V. Sidelev, M.S. Syrtanov, C. Tang, M. Steinbrück, Oxidation kinetics of Cr-coated zirconium alloy: effect of coating thickness and microstructure, Corros. Sci. 175 (2020), 108883.
[17] L.B. Begrambekov, A.E. Evsin, A.V. Grunin, A.I. Gumarov, A.S. Kaplevsky, N. F. Kashapov, A.G. Luchkin, I.R. Vakhitov, I.V. Yanilkin, L.R. Tagirov, Irradiation with hydrogen atoms and ions as an accelerated hydrogenation test of zirconium alloys and protective coatings, Int. J. Hydrog. Energy 44 (2019) 17154–17162.
[18] X. Han, C. Chen, Y. Tan, W. Feng, S. Peng, H. Zhang, A systematic study of the oxidation behavior of Cr coatings on Zry4 substrates in high temperature steam environment, Corros. Sci. 174 (2020), 108826.
[19] J. Yang, U. Stegmaier, C. Tang, M. Steinbrück, M. Große, S. Wang, H.J. Seifert, High temperature Cr-Zr interaction of two types of Cr-coated Zr alloys in inert gas environment, J. Nucl. Mater. 547 (2021), 152806.

[20] X. Wu, W. Li, Y. Wang, Y. Zhang, W. Tian, G. Su, S. Qiu, T. Liu, Y. Deng, H. Huang, Preliminary safety analysis of the PWR with accident-tolerant fuels during severe accident conditions, Ann. Nucl. Energy 80 (2015) 1–13.
[21] J.C. Brachet, T. Guilbert, M. Lesaux, J. Rousselot, G. Nony, C. Toffolon-Masclet, F. Schuster, H. Palancher, J. Bischoff, J. Augereau. Behavior of cr-coated m5 claddings during and after high temperature steam oxidationfrom 800c up to 1500c, Topfuel 2018, 2018.
[22] J. Krejčí, J. Kabátová, F. Manoch, J. Kočí, L. Cvrček, J. Málek, S. Krum, P. Šutta, P. Bublíková, P. Halodová, H.K. Namburi, M. Ševeček, Development and testing of multicomponent fuel cladding with enhanced accidental performance, Nucl. Eng. Technol. 52 (2020) 597–609.
[23] M. Steinbrück, Oxidation of boron carbide at high temperatures, J. Nucl. Mater. 336 (2005) 185–193.
[24] K.L. Lin, C.C. Lin, Zirconia-related phases in the zirconia/titanium diffusion couple after annealing at 1100°–1550° C, J. Am. Ceram. Soc. 88 (2005) 2928–2934.
[25] M. Amaya, F. Nagase, The relationship between the amount of oxidation and activation energy on the steam oxidation reaction of Zircaloy-4 cladding, J. Nucl. Mater. 440 (2013) 457–466.
[26] J. Liu, Z. Cui, Z. Hao, D. Ma, J. Lu, Y. Cui, C. Li, W. Liu, S. Xie, P. Hu, Steam oxidation of Cr-coated Sn-containing Zircaloy solid rod at 1000° C, Corros. Sci. 190 (2021), 109682.
[27] A.M. Huntz, Stresses in NiO, Cr2O3 and Al2O3 oxide scales, Mater. Sci. Eng.: A 201 (1995) 211–228.
[28] H. Ma, J. Yan, Y. Zhao, T. Liu, Q. Ren, Y. Liao, J. Zuo, G. Liu, M. Yao, Oxidation behavior of Cr-coated zirconium alloy cladding in high-temperature steam above 1200 °C, npj Mater. Degrad. 5 (2021) 1–11.
[29] S.C. Tsa, A.M. Huntz, J. Philibert, Diffusion of54Cr and18O in Cr2O 3 scales and growth mechanism, Defect Diffus. Forum 143 (1997) 1195–1200.
[30] B.A. PINT, Experimental observations in support of the dynamic-segregation theory to explain the reactive-element effect, Oxid. Met. 45 (1996) 1–37.
[31] S.C. Tsai, A.M. Huntz, C. Dolin, Growth mechanism of Cr2O3 scales: oxygen and chromium diffusion, oxidation kinetics and effect of yttrium, Mater. Sci. Eng.: A 212 (1996) 6–13.
[32] W.C. Hagel, Anion Diffusion in α-Cr2O3, J. Am. Ceram. Soc. 48 (1965) 70–75.
[33] W. Xiang, S. Ying. Reaction diffusion in chromium-zircaloy-2 system, China Nuclear Information Centre, 2001.
[34] J. Ribis, A. Wu, J.C. Brachet, F. Barcelo, B. Arnal, Atomic-scale interface structure of a Cr-coated Zircaloy-4 material, J. Mater. Sci. 53 (2018) 9879–9895.
[35] A. Wu, J. Ribis, J. Brachet, E. Clouet, F. Leprêtre, E. Bordas, B. Arnal, HRTEM and chemical study of an ion-irradiated chromium/zircaloy-4 interface, J. Nucl. Mater. 504 (2018) 289–299.
[36] I. Barin, Thermochemical Data of Pure Substances, VCH, 1989.
[37] H.X. Zhang, D. Fruchart, E.K. Hlil, L. Ortega, Z.K. Li, J.J. Zhang, J. Sun, L. Zhou, Crystal structure, corrosion kinetics of new zirconium alloys and residual stress analysis of oxide films, J. Nucl. Mater. 396 (2010) 65–70.
[38] L. Royer, X. Ledoux, S. Mathieu, P. Steinmetz, On the oxidation and nitridation of chromium at 1300 °C, Oxid. Met. 74 (2010) 79–92.
[39] H. Asteman, J.E. Svensson, M. Norell, L.G. Johansson, Influence of water vapor and flow rate on the high-temperature oxidation of 304L; effect of chromium oxide hydroxide evaporation, Oxid. Met. 54 (2000) 11–26.
[40] S. Mahboubi, H.S. Zurob, G.A. Botton, J.R. Kish, Effect of water vapour partial pressure on the chromia (Cr2O3)-based scale stability, Can. Metall. Quart. 57 (2018) 89–98.
[41] C. Lemaignan, 2.07 – zirconium alloys: properties and characteristics, in: Comprehensive Nuclear Materials, 2012, pp. 217–232.
[42] J.P. Abriata, J. Garces, R. Versaci, The O–Zr (oxygen-zirconium) system, Bull. Alloy Phase Diagr. 7 (1986) 116–124.
[43] E.C. Subbarao, H.S. Maiti, K.K. Srivastava, Martensitic transformation in zirconia, Phys. Status Solidi (a) 21 (1) (1974) 9–40.
[44] Y. Ikuma, Y. Tsubaki, T. Masaki, Oxygen diffusion in Y2O3-containing tetragonal zirconia polycrystals with different grain sizes, J. Ceram. Soc. Jpn. 99 (1991) 101–103.
[45] M. Steinbrueck, Oxidation of zirconium alloys in oxygen at high temperatures up to 1600C, Oxid. Met. 70 (2008) 317–329.